

# Nonlinear rise in Greenland runoff in response to post-industrial Arctic warming

Luke D. Trusel<sup>1,2\*</sup>, Sarah B. Das<sup>2</sup>, Matthew B. Osman<sup>3</sup>, Matthew J. Evans<sup>4</sup>, Ben E. Smith<sup>5</sup>, Xavier Fettweis<sup>6</sup>, Joseph R. McConnell<sup>7</sup>, Brice P. Y. Noël<sup>8</sup> & Michiel R. van den Broeke<sup>8</sup>

**The Greenland ice sheet (GrIS) is a growing contributor to global sea-level rise<sup>1</sup>, with recent ice mass loss dominated by surface meltwater runoff<sup>2,3</sup>. Satellite observations reveal positive trends in GrIS surface melt extent<sup>4</sup>, but melt variability, intensity and runoff remain uncertain before the satellite era. Here we present the first continuous, multi-century and observationally constrained record of GrIS surface melt intensity and runoff, revealing that the magnitude of recent GrIS melting is exceptional over at least the last 350 years. We develop this record through stratigraphic analysis of central west Greenland ice cores, and demonstrate that measurements of refrozen melt layers in percolation zone ice cores can be used to quantifiably, and reproducibly, reconstruct past melt rates. We show significant ( $P < 0.01$ ) and spatially extensive correlations between these ice-core-derived melt records and modelled melt rates<sup>5,6</sup> and satellite-derived melt duration<sup>4</sup> across Greenland more broadly, enabling the reconstruction of past ice-sheet-scale surface melt intensity and runoff. We find that the initiation of increases in GrIS melting closely follow the onset of industrial-era Arctic warming in the mid-1800s, but that the magnitude of GrIS melting has only recently emerged beyond the range of natural variability. Owing to a nonlinear response of surface melting to increasing summer air temperatures, continued atmospheric warming will lead to rapid increases in GrIS runoff and sea-level contributions.**

Melting across higher elevations of the GrIS results in liquid water infiltration, percolation, and either refreezing or storage within the porous firn layer. Such processes reduce ice-sheet surface albedo, increase firn temperatures<sup>7</sup>, and may generate impermeable ice layers that exacerbate ice-sheet runoff<sup>8</sup>, the proportion of surface melt leaving the ice sheet. Runoff across the margins of the GrIS is presently the leading source of mass loss from the ice sheet<sup>2,3,6</sup>, and has been implicated in the centennial-scale slowdown of the overturning circulation in the North Atlantic Ocean<sup>9</sup>.

GrIS surface melting in 2012 was more expansive than at any time over the 40 years since we started measuring melt using satellites (in 1978)<sup>4</sup>. Proposed mechanisms driving melt in 2012 include contributions from anomalous radiative<sup>10–12</sup> and non-radiative<sup>13</sup> energy fluxes, and anticyclonic atmospheric circulation favouring advection of warm, dry air and clear sky conditions<sup>14</sup>. An ice core record from Summit Station (Fig. 1) demonstrated the exceptional nature of 2012 melt at high elevation (about 3,200 m), revealing<sup>15</sup> that it last occurred at this site in 1889. At lower elevations, where melt occurs more frequently and at greater rates, there exist only limited ice-core-derived reconstructions of melt variability<sup>16–18</sup> and no quantifiable ice-core-based reconstructions of melt intensity or runoff. Furthermore, large discrepancies among reanalysis products over Greenland before the mid-twentieth century<sup>6,19</sup> limit their utility over longer timescales. Consequently, the true anomaly of recent melt intensity and runoff, and the longer-term evolution of these processes in response to climate forcing, remain poorly constrained.

Here we analyse refrozen melt layer stratigraphy in ice cores from central west Greenland (CWG) drilled between 2003 and 2015 to quantify annual melting over the last several centuries (Methods; Extended Data Fig. 1a). Significant co-variability between records from two cores separated by about 40 km in the western GrIS accumulation area (cores GC and D5; Fig. 1) indicates that regional melt, percolation and refreezing are well preserved and represented in these multi-century cores (Fig. 2 inset; Methods). We combine records from cores GC and D5 with a shallower core (core GW; Fig. 1, Extended Data Fig. 1b) to create a single 339-year stacked CWG record (Methods). CWG reveals frequent, but generally low-magnitude, melting during the last three centuries, with approximately 13-year periodicity and a marked departure from low-melt conditions over the last two decades (Fig. 2). We develop a complementary 364-year melt record using a fourth core (core NU) recovered from an ice cap on Nuussuaq Peninsula (Fig. 1) in 2015. The NU core record contains a greater overall magnitude of melt than the CWG combined core record owing to its lower elevation and coastal location (Extended Data Table 1), similar 13–16-year oscillations, and a distinct departure from baseline conditions in recent decades (Fig. 2). Common periodicities in the CWG and NU melt records suggest the influence of multiple known climate modes on melt variability (Extended Data Fig. 2; Methods). In all cores, there is also a clear pattern towards more frequent, thicker (and thus more intense) melt layers towards the present day (Extended Data Fig. 1c).

Our results show a pronounced 250% to 575% increase in melt intensity over the last 20 years, relative to a pre-industrial baseline period (eighteenth century) for cores NU and CWG, respectively (Fig. 2). Furthermore, the most recent decade contained in the cores (2004–2013) experienced a more sustained and greater magnitude of melt than any other 10-year period in the ice-core records. For GrIS cores, 2012 melt is unambiguously the strongest melt season on record. Both NU and CWG annual ice-core-derived melt records significantly ( $P < 0.01$ ) correlate with one another over their 339 years of overlap, and both also with summer air temperatures from the Ilulissat region (Extended Data Table 2; Methods), relationships that improve after applying a 5-year moving average, probably reflecting the noise inherent to melt records owing to variability in meltwater percolation and refreezing<sup>8,16</sup>. These empirically derived results revealing coherence between independent melt and temperature records emphasize broad-scale GrIS melt forcing, and suggest that summer warming (see Fig. 2) is an important component of the observed regional melt intensification.

GrIS ice cores provide a valuable point-scale view of melt history within the percolation zone, but records of past melt variability within the GrIS saturation and bare ice zones, where melt is more directly tied to mass loss and runoff, have remained elusive. To assess whether our ice-core-derived melt records also serve as quantitative archives of past regional-scale melt variability and intensity, we examine correlations between the CWG stack and recent modelled and observed melt parameters across the entire GrIS (Fig. 3; Methods). We find

<sup>1</sup>Department of Geology, Rowan University, Glassboro, NJ, USA. <sup>2</sup>Department of Geology and Geophysics, Woods Hole Oceanographic Institution, Woods Hole, MA, USA. <sup>3</sup>Joint Program in Oceanography, Massachusetts Institute of Technology/Woods Hole Oceanographic Institution, Woods Hole, MA, USA. <sup>4</sup>Department of Chemistry, Wheaton College, Norton, MA, USA. <sup>5</sup>Polar Science Center, Applied Physics Laboratory, University of Washington, Seattle, WA, USA. <sup>6</sup>Department of Geography, University of Liège, Liège, Belgium. <sup>7</sup>Division of Hydrologic Sciences, Desert Research Institute, Reno, NV, USA. <sup>8</sup>Institute for Marine and Atmospheric Research, Utrecht University, Utrecht, Netherlands. \*e-mail: trusel@rowan.edu

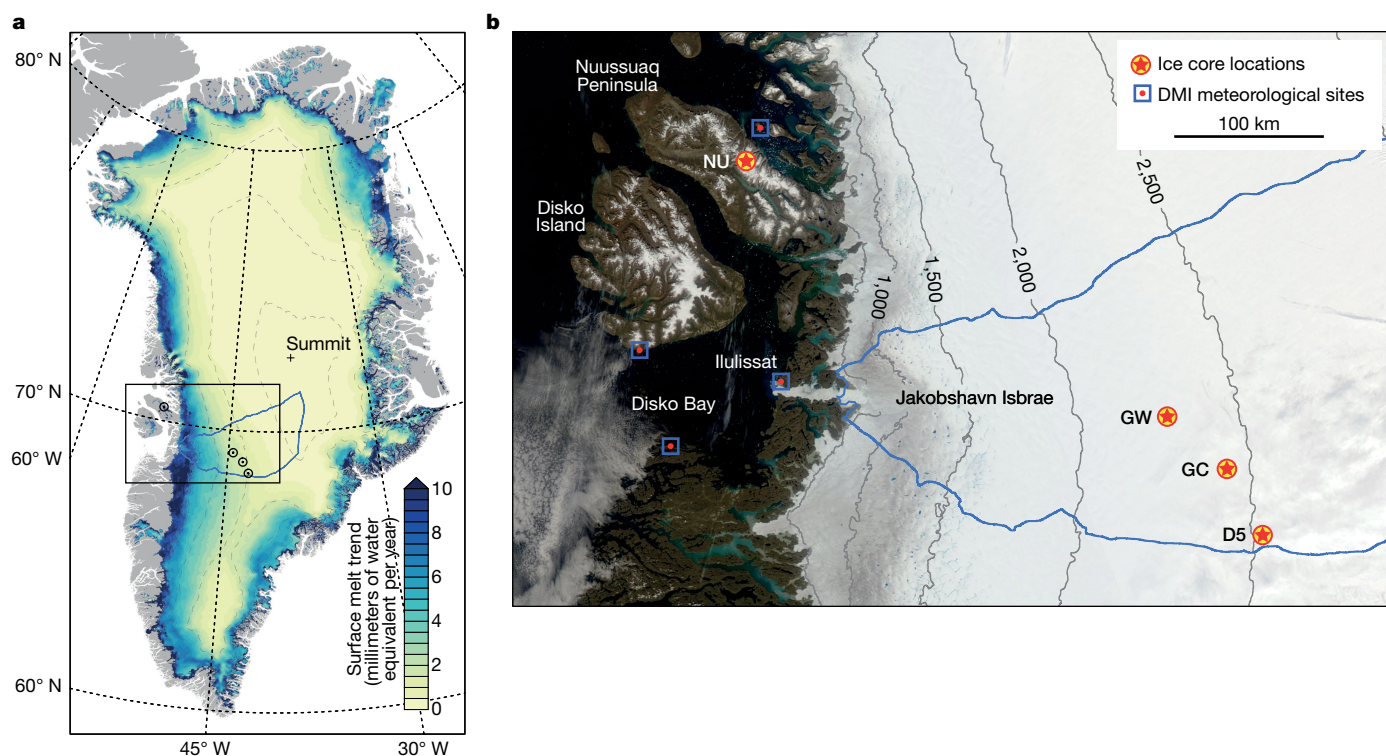


**Fig. 1 | Positive trends in Greenland surface melt and locations of ice cores used to reconstruct past surface melt variability.** **a**, Positive trends in annual surface meltwater production over 1958–2016, as simulated by RACMO2.3p2<sup>5</sup>. **b**, Locations of our ice cores situated within the Jakobshavn drainage basin (blue outline; basin 7.1) of CWG and on the

Nuussuaq Peninsula, as well as air-temperature observations integrated into a composite Ilulissat air-temperature record (Methods; Extended Data Table 2). The satellite image in **b** was obtained with the NASA MODIS instrument (from the NASA Rapid Response data archive).

wide-ranging significant ( $P < 0.01$ ) positive correlations between the CWG melt record and RACMO2-modelled<sup>5</sup> melt (Fig. 3a) and refreezing (Fig. 3b), as well as satellite-observed melt duration<sup>4</sup> (Fig. 3d). Further supporting these results are significant ( $P < 0.01$ ) relationships between our NU and CWG melt records and long-term pan-Greenland air temperature observations (Extended Data Table 3; Methods). Moreover, we find significant ( $P < 0.01$ ) and wide-ranging correlations

between the ice-core-derived melt record and RACMO2-simulated meltwater runoff across the ice-sheet margins (Fig. 3c). These ice-core model relationships indicate that rates of meltwater production, refreezing and runoff across much of Greenland are all at multi-century highs, assuming that the spatial character of melt and high correlations between modelled GRIS-integrated melt, refreezing, and runoff are robust and have remained stationary through time (Extended Data Fig. 4).

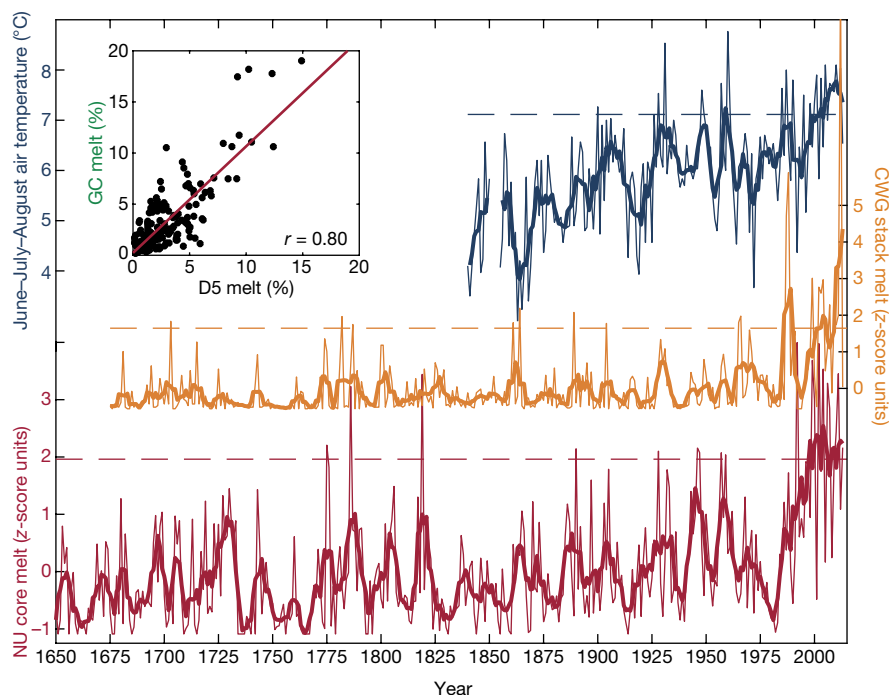


**Fig. 2 | Multi-century evolution of CWG surface melt from ice cores.** Observed summer (June–August) air temperatures from the Ilulissat area and melt intensity (in standardized z-score units) from the CWG ice-core-derived melt stack and from the NU core on Nuussuaq Peninsula (see Methods). Horizontal dashed lines show means over the last twenty years of the ice-core records (1994–2013). Bold lines show 5-year smoothed time series. Significant correlation ( $P < 0.01$ ;  $n^* = 106$ ) between 5-year running means of GC and D5 melt per cent (inset) reveals that variability in total annual surface melt, as well as broader regional melt variability, is well captured by our ice cores.

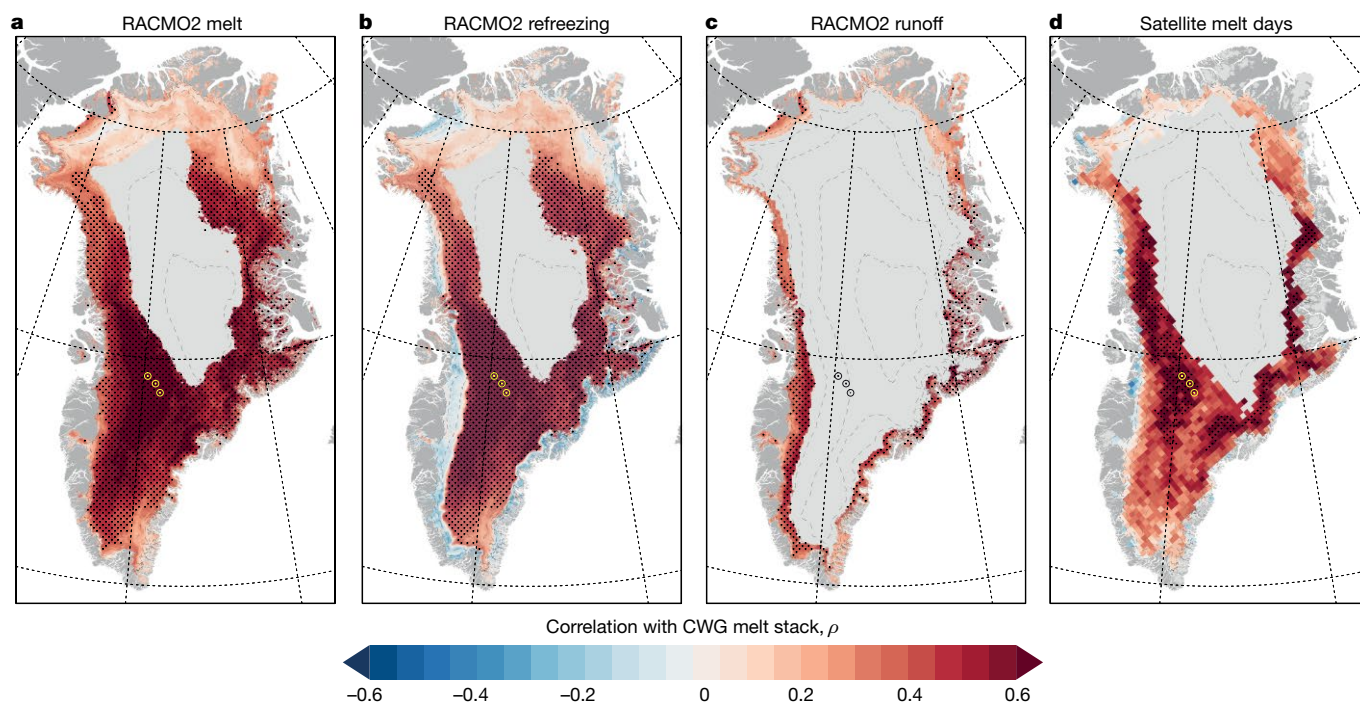


**Fig. 3 | Spatially broad representation of melt processes captured by CWG ice cores.** **a–d**, Spearman rank order correlations between the CWG melt stack and RACMO2-modelled annual melt (**a**), refreezing (**b**) and runoff (**c**) over 1958–2013<sup>5</sup>, and with satellite-observed melt over 1988–2013<sup>4</sup> (**d**; Methods). Areas of significant correlation ( $P < 0.01$ ) are

denoted by the black stipple pattern. Correlations are calculated only for years where the gridded data indicated melt for  $>50\%$  of the years (28 years in **a–c**; 13 years in **d**). The location of cores used in the CWG stack is denoted by yellow (**a**, **b**, **d**) or black (**c**) points. Contour interval, 500 m.

Given the strong correlations between modern percolation zone melt and ice-sheet meltwater runoff, we produce the first observationally constrained record of ice-sheet runoff variability using a stepwise calibration/validation procedure between our ice-core melt records and RACMO2 runoff (Methods). Performing this analysis against integrated runoff from each GrIS surface drainage basin (Extended Data Fig. 5), as well as total GrIS runoff (Fig. 4a), we find that the combined CWG and NU melt records possess high predictive skill in reconstructing runoff over 1958–2013 across much of the GrIS (Extended Data Figs. 5, 6). Our results show that relatively stable and low runoff occurred before the 1990s in all individual basins (Extended Data Fig. 5) as well as across the broader ice sheet. Our reconstructions are consistent with modern model-based runoff estimates (Fig. 4a) and limited direct runoff measurements<sup>20</sup>. Divergence in past runoff estimates derived from longer reanalyses<sup>6,19</sup> hinders centennial-scale comparisons, but also highlights in particular the value of our new observationally based reconstruction farther back in time. We show that an exceptional rise in runoff has occurred over the last two decades, equating to an approximately 50% increase in GrIS-integrated runoff compared to pre-industrial runoff, and a 33% increase over the twentieth century alone (Fig. 4a).

The onset of industrial-era Arctic warming occurred in the mid-nineteenth century<sup>21</sup> and differential smoothing analysis likewise indicates increases in GrIS runoff initiated shortly thereafter (Fig. 4b; Methods). The median onset of positive trends in GrIS runoff are also coincident with the median onset of weakening Atlantic meridional overturning circulation<sup>9</sup>. Emergence of runoff beyond the natural range of variability, however, has only very recently occurred (Fig. 4b). Although the precise mechanisms behind these rapid recent changes remain unconstrained, the high temporal resolution of our reconstruction allows us to explore a range of possibilities. Runoff emergence timing follows the emergence (that is, steep decline) of pan-Arctic summer sea ice (Methods; Fig. 4b, Extended Data Table 4), supporting prior hypotheses that Arctic sea ice loss may amplify GrIS melt and runoff<sup>22</sup>. The pronounced sea ice and runoff changes are also roughly coincident with a negative shift in the summer North Atlantic Oscillation, marking

enhanced summertime anticyclonic conditions over Greenland known to contribute to warming<sup>23</sup> and a positive melt–albedo feedback<sup>12</sup>. Sea-ice loss is also suggested to be more directly responsible for atmospheric blocking over Greenland, thus contributing to recent North Atlantic Oscillation trends<sup>22</sup>. Regional atmospheric<sup>24</sup> and sea-ice<sup>25</sup> trends may also represent a teleconnected pan-Arctic response to tropical Pacific sea surface temperature forcing.

Our reconstruction quantifies the exceptional magnitude of present-day melt and runoff relative to the last several centuries. Their rapid intensification over the last two decades also illustrates a clear non-linear melt–temperature relationship (Fig. 4c; Methods). Similar late-twentieth-century melt acceleration was found using records from an Antarctic Peninsula ice core<sup>26</sup>, and attributed to a nonlinear response of melting to climate warming more broadly across Antarctica, owing largely to the melt–albedo positive feedback<sup>27</sup>. At all of our core sites, 2012 melt was more intense than any other year according to two distinct reanalysis-forced regional climate models that extend back to 1958<sup>5</sup> and 1979<sup>6</sup> (Fig. 4c). Our ice-core results provide further context and reveal that these 2012 melt rates are exceptional highs for at least the past 350 years. If an air-temperature reconstruction from the nearby Canadian Arctic is regionally representative, GrIS melt and runoff experienced in the last decade is likely also to be unprecedented over the last 6,800–7,800 years<sup>28</sup>. The nonlinear melt–temperature sensitivity also helps explain why episodes of mid-twentieth-century warmth resulted in less intense and less sustained melting compared to the last two decades, despite being only marginally cooler (Fig. 2). Additional factors, such as recent sea-ice losses, as well as regional and teleconnected general circulation changes, may also play a part in amplifying the melt response. Moreover, this melt–temperature nonlinearity indicates that only limited additional warming will greatly enhance the area of the ice sheet subject to meltwater runoff. Indeed, even high-elevation regions of the percolation zone, such as at our CWG core sites, have already warmed enough to induce the melt intensification and firn densification necessary to generate meltwater runoff in some years, as opposed to full melt refreezing and retention (Fig. 4c).

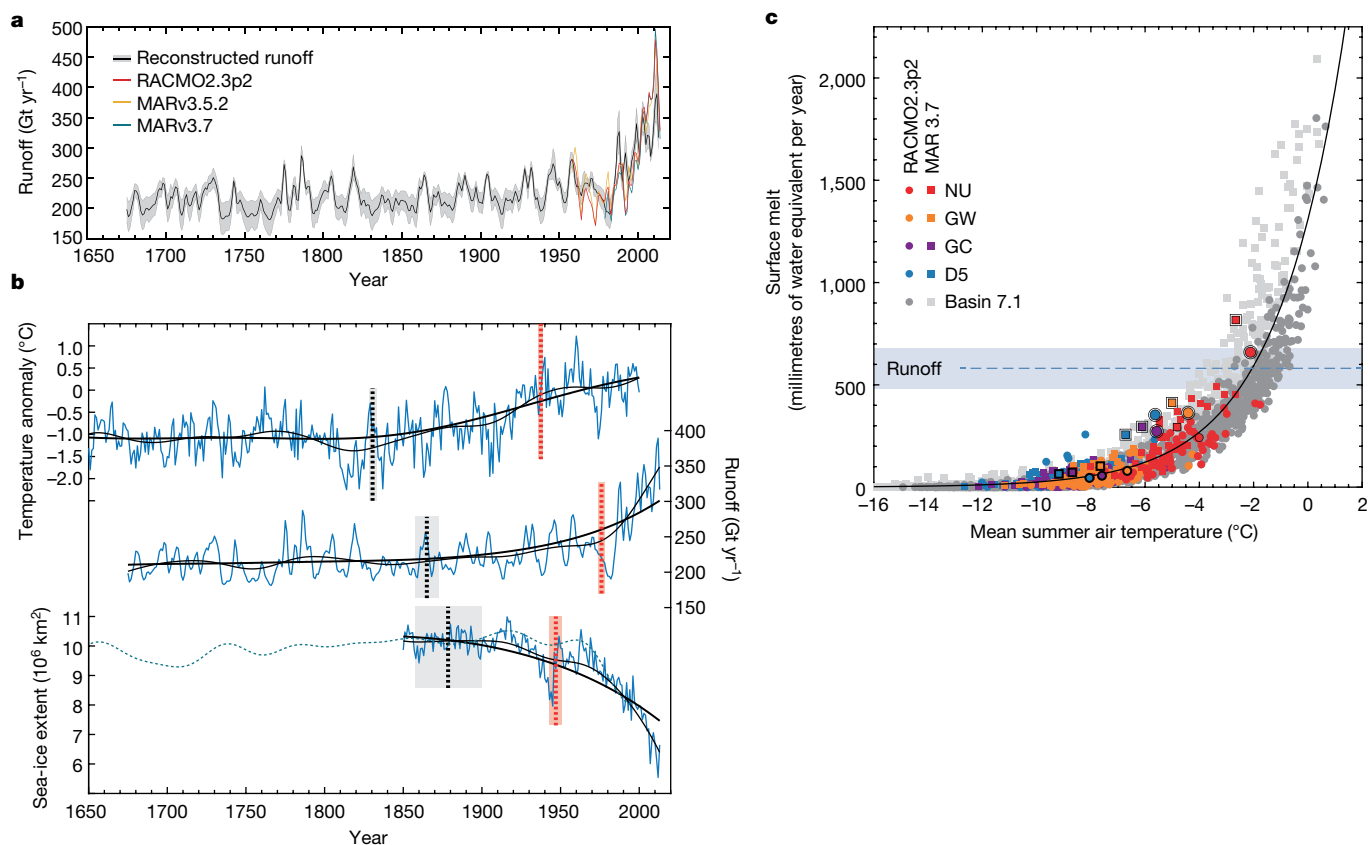


**Fig. 4 | Exceptional rise in Greenland ice-sheet runoff and climate warming context.** **a**, GrIS-integrated meltwater runoff, as simulated by regional climate models<sup>5,6</sup> (coloured lines; 5-year smoothed) and reconstructed using the NU and CWG ice-core-derived melt records (black line; 95% confidence interval shaded; see Methods). **b**, Median onset of significant trends (vertical black dotted lines) and climate emergence above pre-industrial (vertical red dotted lines) for mean Arctic temperatures<sup>21</sup> (top), our ice-core-derived runoff reconstruction (middle) and two summer Arctic sea-ice extent datasets<sup>29,30</sup> (bottom; Methods). Median absolute deviations of trend onsets and climate emergence shown as shaded boxes. Thin and bold black lines denote 15-year and 50-year Gaussian smoothed series. **c**, Recent modelled evolution of mean summer (JJA) near-surface air temperature and surface

melt (in millimetres of water equivalent per year) across CWG. Ice core sites are shown as coloured points, and a Jakobshavn basin (basin 7.1; Fig. 1) elevational transect as grey points from RACMO2.3p2 (circles) and MARv3.7 (squares). Means over the past 20 years of the ice-core records (1994–2013) at core sites are denoted by points with single black border, and peak melting in 2012 by double black borders. The evolution of CWG ice-sheet melt in response to a warming climate is well represented by an exponential function (black curve). Recent melt rates at our percolation zone core sites approach conditions where the models have recently begun to simulate meltwater runoff (blue dashed line indicates mean runoff-linked melt rate and the shaded region corresponds to  $\pm 1$  s.d.; see Methods for details).

Our GrIS melt and runoff reconstructions highlight how ice-core-based surface mass balance reconstructions add important additional in situ context to the relatively brief instrumental, satellite and climate reanalysis eras. Today, surface melting and melt-induced runoff in Greenland occur at magnitudes not previously experienced over at least the last several centuries, if not millennia. Melt–temperature nonlinearity and general circulation changes mean that further twenty-first-century warming has important implications for the ice-sheet mass balance, by accelerating the intensity of surface melting and amplifying GrIS contributions to global sea-level rise.

### Online content

Any methods, additional references, Nature Research reporting summaries, source data, statements of data availability and associated accession codes are available at <https://doi.org/10.1038/s41586-018-0752-4>.

Received: 4 May; Accepted: 18 September 2018;  
Published online 5 December 2018.

- Hanna, E. et al. Ice-sheet mass balance and climate change. *Nature* **498**, 51–59 (2013).
- Enderlin, E. M. et al. An improved mass budget for the Greenland ice sheet. *Geophys. Res. Lett.* **41**, 2013GL059010 (2014).
- van den Broeke, M. R. et al. On the recent contribution of the Greenland ice sheet to sea level change. *Cryosphere* **10**, 1933–1946 (2016).

- Tedesco, M. et al. Evidence and analysis of 2012 Greenland records from spaceborne observations, a regional climate model and reanalysis data. *Cryosphere* **7**, 615–630 (2013).
- Noël, B. et al. Modelling the climate and surface mass balance of polar ice sheets using RACMO2—Part 1: Greenland (1958–2016). *Cryosphere* **12**, 811–831 (2018).
- Fettweis, X. et al. Reconstructions of the 1900–2015 Greenland ice sheet surface mass balance using the regional climate MAR model. *Cryosphere* **11**, 1015–1033 (2017).
- Humphrey, N. F., Harper, J. T. & Pfeffer, W. T. Thermal tracking of meltwater retention in Greenland's accumulation area. *J. Geophys. Res.* **117**, F01010 (2012).
- Machguth, H. et al. Greenland meltwater storage in firn limited by near-surface ice formation. *Nat. Clim. Chang.* **6**, 390–393 (2016).
- Thornalley, D. J. R. et al. Anomalously weak Labrador Sea convection and Atlantic overturning during the past 150 years. *Nature* **556**, 227–230 (2018).
- Bennartz, R. et al. July 2012 Greenland melt extent enhanced by low-level liquid clouds. *Nature* **496**, 83–86 (2013).
- Van Tricht, K. et al. Clouds enhance Greenland ice sheet meltwater runoff. *Nat. Commun.* **7**, 10266 (2016).
- Hofer, S., Tedstone, A. J., Fettweis, X. & Bamber, J. L. Decreasing cloud cover drives the recent mass loss on the Greenland Ice Sheet. *Sci. Adv.* **3**, e1700584 (2017).
- Fausto, R. S. et al. The implication of nonradiative energy fluxes dominating Greenland ice sheet exceptional ablation area surface melt in 2012. *Geophys. Res. Lett.* **43**, 2649–2658 (2016).
- Hanna, E. et al. Atmospheric and oceanic climate forcing of the exceptional Greenland ice sheet surface melt in summer 2012. *Int. J. Climatol.* **34**, 1022–1037 (2014).

15. Keegan, K. M., Albert, M. R., McConnell, J. R. & Baker, I. Climate change and forest fires synergistically drive widespread melt events of the Greenland Ice Sheet. *Proc. Natl Acad. Sci. USA* **111**, 7964–7967 (2014).
16. Graeter, K. A. et al. Ice core records of West Greenland melt and climate forcing. *Geophys. Res. Lett.* **45**, 3164–3172 (2018).
17. Herron, M. M., Herron, S. L. & Langway, C. C. Climatic signal of ice melt features in southern Greenland. *Nature* **293**, 389–391 (1981).
18. Kameda, T. et al. Melt features in ice cores from Site J, southern Greenland: some implications for summer climate since AD 1550. *Ann. Glaciol.* **21**, 51–58 (1995).
19. van den Broeke, M. et al. Greenland ice sheet surface mass loss: recent developments in observation and modeling. *Curr. Clim. Change Rep.* **3**, 345–356 (2017).
20. Ahlström, A. P., Petersen, D., Langen, P. L., Citterio, M. & Box, J. E. Abrupt shift in the observed runoff from the southwestern Greenland ice sheet. *Sci. Adv.* **3**, e1701169 (2017).
21. Abram, N. J. et al. Early onset of industrial-era warming across the oceans and continents. *Nature* **536**, 411–418 (2016).
22. Liu, J. et al. Has Arctic sea-ice loss contributed to increased surface melting of the Greenland ice sheet? *J. Clim.* **29**, 3373–3386 (2016).
23. Fettweis, X. et al. Brief communication 'Important role of the mid-tropospheric atmospheric circulation in the recent surface melt increase over the Greenland ice sheet'. *Cryosphere* **7**, 241–248 (2013).
24. Ding, Q. et al. Tropical forcing of the recent rapid Arctic warming in northeastern Canada and Greenland. *Nature* **509**, 209–212 (2014).
25. Ding, Q. et al. Influence of high-latitude atmospheric circulation changes on summertime Arctic sea ice. *Nat. Clim. Chang.* **7**, 289–295 (2017).
26. Abram, N. J. et al. Acceleration of snow melt in an Antarctic Peninsula ice core during the twentieth century. *Nat. Geosci.* **6**, 404–411 (2013).
27. Trusel, L. D. et al. Divergent trajectories of Antarctic surface melt under two twenty-first-century climate scenarios. *Nat. Geosci.* **8**, 927–932 (2015).
28. Lecavalier, B. S. et al. High Arctic Holocene temperature record from the Agassiz ice cap and Greenland ice sheet evolution. *Proc. Natl Acad. Sci. USA* **114**, 5952–5957 (2017).
29. Walsh, J. E., Fetterer, F., Scott Stewart, J. & Chapman, W. L. A database for depicting Arctic sea ice variations back to 1850. *Geogr. Rev.* **107**, 89–107 (2017).
30. Kinnard, C. et al. Reconstructed changes in Arctic sea ice over the past 1,450 years. *Nature* **479**, 509–512 (2011).

**Acknowledgements** Funding was provided by US National Science Foundation (NSF) awards OPP-1205196 and PLR-1418256 to S.B.D., ARC-1205062 to B.E.S. and OPP-1205008 to M.J.E. L.D.T. acknowledges institutional support from Rowan University and the Doherty Postdoctoral Scholarship at Woods Hole Oceanographic Institution. M.B.O. acknowledges support from the Department of Defense Office of Naval Research, National Defense Science and Engineering Graduate (NDSEG) Fellowship, 32 CFR 168a. Collection,

analysis and interpretation of core D5 was supported by NSF grant 0352511 to J.R.McC. B.P.Y.N. and M.R.v.d.B. acknowledge support from the Polar Program of the Netherlands Organization for Scientific Research (NWO/NPP) and the Netherlands Earth System Science Centre (NESSC). For running the MAR model, computational resources have been provided by the Consortium des Équipements de Calcul Intensif (CÉCI), funded by the Fonds de la Recherche Scientifique de Belgique (FRS-FNRS) under grant number 2.5020.11 and the Tier-1 supercomputer (Zenobe) of the Fédération Wallonie Bruxelles infrastructure funded by the Walloon Region under grant agreement number 1117545. We thank M. Waszkiewicz and IDPO/IDDO for ice core drilling support. We thank the NSF Ice Core Facility (formerly NICL), A. York, M. Bingham, M. Hatch, S. Zarfos, Z. Li, and Milton Academy students for ice core sampling and processing support. We thank R. Banta for help with the D5 core, and A. Arienzo and N. Chellman for help in analysing the NU core. We thank M. Tedesco for providing the satellite melt duration data used in Fig. 3d. Maps in Figs. 1a, 3 and Extended Data Figs. 3, 4 were created with the NCAR Command Language (<https://www.ncl.ucar.edu>), and maps in Fig. 1b and Extended Data Fig. 6 were created with Esri ArcGIS. We acknowledge the use of Rapid Response imagery in Fig. 1b from the Land, Atmosphere Near real-time Capability for EOS (LANCE) system operated by the NASA/GSFC/Earth Science Data and Information System (ESDIS) with funding provided by NASA/HQ.

**Reviewer information** *Nature* thanks J. Briner and B. Vinther for their contribution to the peer review of this work.

**Author contributions** L.D.T. and S.B.D. conceived of and designed the study with input from M.B.O. B.E.S., S.B.D., M.J.E. and L.D.T. determined the ice core siting. S.B.D., L.D.T., M.B.O. and M.J.E. collected the ice cores. L.D.T. analysed melt stratigraphy for cores NU, GC and GW. S.B.D., J.R.McC. and L.D.T. analysed core D5. M.J.E. and J.R.McC. analysed ice core chemistry. Ice core chronology was led by M.B.O. with input from B.E.S., S.B.D., J.R.McC. and L.D.T. M.B.O. developed melt reconstruction code with input from L.D.T. B.P.Y.N. and M.R.v.d.B. provided RACMO2 model output and expertise. X.F. provided MAR model output and expertise. L.D.T. led the data analyses and interpretation, and wrote the manuscript, with input from S.B.D. and M.B.O. All authors read and commented on the manuscript.

**Competing interests** The authors declare no competing interests.

#### Additional information

**Extended data** is available for this paper at <https://doi.org/10.1038/s41586-018-0752-4>.

**Reprints and permissions information** is available at <http://www.nature.com/reprints>.

**Correspondence and requests for materials** should be addressed to L.D.T.

**Publisher's note:** Springer Nature remains neutral with regard to jurisdictional claims in published maps and institutional affiliations.

## METHODS

**Ice-core melt analyses.** Surface melt histories were developed from an array of percolation-zone firn and ice cores collected in CWG (Figs. 1, 2, Extended Data Table 1). Core chronology was achieved through annual layer counting of seasonal ice-core chemistry (including the summertime species  $\delta^{18}\text{O}$ ,  $\text{NO}_3^-$  and  $\text{SO}_4^{2-}$ , and the winter/springtime species  $\text{Mg}^{2+}$ ,  $\text{Ca}^{2+}$  and  $\text{Na}^+$ ) for cores GC and GW. Soluble chemistry measurements were conducted on discrete, 5-cm-long longitudinal cuts for both cores using suppressed ion chromatography<sup>31</sup>. The relative dating uncertainty in the GW and GC cores is estimated at a year or less, based on validation of the annual layer counts with absolute-dated volcanic horizons<sup>32</sup>. In the NU core, simultaneous and depth-registered measurements of trace metallic species (Na, Mg, S, Cl, Ca, Br, Sr, Ce, Ti and Pb), black carbon, water isotopic abundance ( $\delta^{18}\text{O}$  and  $\delta\text{D}$  of  $\text{H}_2\text{O}$ ), as well as semiquantitative particle counts, were conducted at a continuous resolution of about 2 cm (water equivalent) following established methods<sup>33,34</sup>. Annual layer counts were similarly determined in the NU core down to the Huaynaputina (Peru) volcanic horizon<sup>32</sup> at AD 1601, via identification of winter–springtime seasonality in Na, Mg, Ca and particulates<sup>35</sup>, and summertime seasonality in S,  $\delta^{18}\text{O}$ , black carbon and heavy metals<sup>34</sup>. The relative uncertainty down to AD 1601 is estimated at two year or less using validation of annual layer counts with 15 absolute-dated tie points (13 volcanic, 2 radiogenic; following ref.<sup>36</sup>). Reference<sup>34</sup> details the establishment of the depth–age scale for core D5.

All cores were latitudinally cut, cleaned and analysed for visible refrozen stratigraphic horizons at the US National Science Foundation Ice Core Facility, formerly the National Ice Core Laboratory (NICL). Cores GC, GW and NU were scanned with the NICL high-resolution (sub-millimetre) optical imaging system<sup>37</sup>. Resulting images allowed for manual identification of refrozen melt layers using digitally registered core depths (see, for example, Extended Data Fig. 1a). Following established melt layer identification<sup>38</sup> and classification<sup>26</sup> methods, we characterized only horizontally continuous refrozen melt layers with discrete upper and lower bounds identifiable based on their optical contrast with surrounding undisturbed firn or ice, while excluding vertical percolation features or layers extending <50% of the total ice-core width. For core D5, we applied the same methodology to detailed stratigraphic logs produced from analysis of the ice core on a back-lit table at NICL. We report results of these analyses for the full length of the GC, GW and D5 records, and for the upper 86 m of the NU core (corresponding to the year AD 1650), beyond which refrozen melt horizons become ambiguous owing to layer thinning and reduced visible contrast between refrozen layers and surrounding ice. As annual accumulation and melt layers advect downward, thinning of both annual accumulation and melt layers occurs<sup>26,39</sup>. It is therefore necessary to account for this thinning as a function of increasing depth, and following previous studies<sup>18,26</sup>, we characterize melt as a percentage of annual snow accumulation after converting each to water equivalent lengths using density measurements along the core and assuming a density of ice ( $0.917\text{ g cm}^{-3}$ ) for refrozen melt layers. After converting melt thicknesses to melt per cent, cores GC, GW and D5 were composited to form the CWG stack by averaging and standardizing (mean set to 0 and standard deviation set to 1) the records. To facilitate comparison, the NU melt per cent record was also standardized based on its full time series (1650–2013). Melt intensity increases were calculated before standardizing.

**Broader spatial representation of ice-core melt histories.** To assess the potential of our ice-core melt records to indicate wider ice-sheet melt variability, we calculated correlations across space between the annual CWG melt stack and gridded model and satellite melt datasets (Fig. 3). To quantify these relationships across space, we assessed Spearman rank order correlations owing to the nonparametric distributions of the datasets as a result of nonlinear melt evolution<sup>26,27</sup> and tested significance (at the  $P < 0.01$  level) using a two-tailed Student's  $t$ -test. Two sophisticated reanalysis-driven regional climate–snowpack models were used in our analysis, as well as satellite-derived estimates of annual surface melt duration. First, the most recent version of RACMO2, RACMO2.3p2, forced by the ECMWF ERA-40 and ERA-Interim reanalyses over 1958–2013 and statistically downscaled to 1 km spatial resolution from 11 km native outputs<sup>5,40</sup>, was used to assess correlations with melt magnitude, refreezing, and runoff (Fig. 3a–c). As an assessment of the sensitivity of these correlations to model selection, we also calculated correlations against the MARv3.7 model forced by ERA-Interim over 1979–2013 and similarly downscaled to 1 km from 7.5 km native outputs<sup>6</sup>. Despite incorporating a unique snow model, results using MARv3.7 show broadly similar results to those from RACMO2.3p2, including wide-ranging significant correlations between the CWG ice-core composite and simulated melt and runoff (Extended Data Fig. 3). We also quantified spatial correlations with observed melting from satellite passive microwave radiometers at 25 km resolution<sup>4,41</sup> over the time period of common overlap with full daily satellite observations (1988–2013), and note similarly high spatial correlations between satellite-observed summer melt duration and melt variability from the ice cores (Fig. 3d). Finally, we report correlations only where the gridded dataset indicated that the respective melt variable occurred in at least 50%

of the years of common overlap (that is, 28 years for the 1958–2013 RACMO2 and 13 years for the 1988–2013 satellite time series).

**Runoff reconstruction.** Ice core-derived runoff reconstructions were performed through multilinear regression of the CWG and NU melt records as predictor (independent) variables against RACMO2-modelled annual runoff as the predictand (dependent variable) over the period of common overlap between the two datasets (1958–2013). This procedure allows us to develop a transfer function by calibrating the ice-core melt records to the RACMO2-simulated runoff, and thus extend the runoff record back in time using only the ice-core melt records. We used a nonparametric Monte Carlo approach to generate 95% confidence intervals to the reconstructions. Namely, we developed 10,000 surrogate pseudo-random predictor/predictand pairings over the full calibration interval (1958–2013) using the frequency-domain method<sup>42</sup>, following established methods<sup>43</sup>. To test reconstruction skill, we calculated the coefficient of determination ( $r^2$ ), reduction of error (RE), and coefficient of efficiency (CE) statistics<sup>44</sup>. Both RE and CE may vary from 1 to  $-\infty$ , where  $\text{RE} > 0$  and  $\text{CE} > 0$  indicate a predictive power above the simple mean estimate of RACMO2-simulated runoff during the calibration interval. Indeed, positive RE and CE values are commonly invoked to demonstrate skillful reconstructions<sup>45,46</sup>. Any positive value of RE and CE, however, does not necessarily signify statistical significance provided the predictor/predictand series represent varying degrees of autocorrelation. Thus, to estimate whether a calibration statistic is significant for the ice-core and RACMO2 data, we additionally used 10,000 Monte Carlo iterations to develop empirical probability density functions for the reconstruction statistics ( $r^2$ , RE, CE) tuned to the exact autocorrelative properties and length of the observed predictor/predictand series, and against which significance was tested<sup>43</sup>. Next, to test the sensitivity of the reconstruction to calibration period, we performed stepwise cross-validation tests<sup>45</sup>. This was done by initially defining the calibration interval as the most recent contiguous two-thirds of years in the period of common overlap between the ice-core and RACMO2 datasets (1977–2013), such that the validation interval initially represented the oldest one-third of available years (1958–1976). The cross-validation calibration interval was then stepped to one year older (1976–2012), while the verification interval was defined as all remaining years (1958–1975, 2013). This was progressively repeated until the calibration interval represented the oldest two-thirds of the period of common overlap (1958–1994) and the verification interval represented the youngest contiguous one-third of years (1995–2013). After each iteration, validation statistics ( $r^2$ , RE, CE) were calculated and significance levels were determined using the Monte Carlo approach described above.

We performed this procedure of multilinear regression between ice-core melt records and RACMO2-modelled runoff, estimation of reconstruction confidence intervals, and iterative calibration period and statistic assessment to reconstruct runoff across each of the 19 ICESat elevation-defined GrIS surface drainage basins<sup>47</sup> and for the ice sheet as a whole (Extended Data Fig. 5). For this analysis, we first smoothed all data series using a 5-year centred moving average, as this allows for the possibility of meltwater percolation to deeper layers (potentially important for the higher-melt NU core) while also remaining consistent with the approximate integral timescale in melt and its climatic drivers across the GrIS. In each case, area-integrated RACMO2 runoff (that is, across a specific basin or entire ice sheet) was used as the predictand and the NU and CWG melt records as predictors.

For most individual basins and for GrIS-integrated runoff (the focus of our study), the majority of calibration intervals produced CE and RE values much greater than zero and significant validation statistics, indicating broad and skillful runoff reconstructions (Extended Data Fig. 6). The northernmost GrIS basins, in particular basins 1 and 8, overall had the fewest calibration/validation intervals where validation statistics ( $r^2$ , RE, CE) were found to be significant, indicating comparatively low skill in reconstructing RACMO2 runoff in this region (Extended Data Fig. 6). However, our ice-core melt records and derived reconstruction of basin 8.2 runoff moderately agree with observed air temperatures from the nearby Pituffik site since 1948 (Extended Data Table 3; also see next section), and our reconstructed late twentieth-century increases in melt across northern Greenland (Extended Data Fig. 5) are consistent with recently rapid warming and melting reported in the Canadian Arctic<sup>28,48</sup>. Robust reconstruction of GrIS-integrated runoff, despite a relatively poor fit with RACMO2 across northern basins is probably the result of little runoff originating from northern Greenland (about 8%–13% on average annually according to RACMO2 and MAR, respectively), and because GrIS-integrated runoff is dominated by runoff from the central-southwestern and southern basins (Extended Data Fig. 5). In these more southerly regions, our runoff reconstruction (Extended Data Figs. 5, 6), relationships between our ice core-derived melt and modelled and satellite-observed melt (Fig. 3, Extended Data Fig. 3), and relationships between point-scale melt processes and GrIS-integrated melt and runoff (Extended Data Fig. 4) are all particularly strong. Nevertheless, collection and integration of compatible ice-core melt records from regions currently under-represented in our reconstruction could

provide an opportunity to improve upon basin-level reconstructions of GrIS melt and runoff.

As an additional check on our runoff reconstruction, we also compared ice-core-reconstructed runoff calibrated using RACMO2 against two versions of the MAR model<sup>6</sup> (v3.5.2 and v3.7), forced by ECMWF reanalyses and down-scaled to 5 km and 1 km resolution, respectively. We note strong agreement at the ice-sheet scale among the models and reconstruction (Fig. 4a). Similar methodological agreement is found across most individual drainage basins, although it is also clear there are biases among the magnitudes of runoff simulated by models in some basins that compensate when integrated over the full GrIS (Extended Data Fig. 5), a feature that has persisted since previous versions of the models<sup>49</sup>.

**Comparisons with observed air temperatures.** As a further assessment of our ice-core melt time series and the derived runoff reconstruction, we quantified relationships between these variables and observed air temperatures across coastal Greenland (Extended Data Table 3). We used data<sup>50,51</sup> compiled and archived by the Danish Meteorological Institute (DMI) for all sites with near-continuous summer (JJA) observations that predate the onset of the ERA-40 reanalysis (1958) used to drive RACMO2 and which extend to at least 2013, the most recent year in the ice core records. As in our runoff reconstruction, we use the CWG and NU melt time series as predictor variables in a multilinear regression against observed air temperatures after calculating 5-year moving averages of the time series. We find overwhelmingly significant (see next section) relationships between the temperature time series and the combined CWG and NU melt records, as well as between reconstructed runoff integrated across surface drainage basins adjacent to the location of air-temperature observations (Extended Data Table 3). We do note, however, that in general stronger peak correlations exist between the ice-core melt records and melt simulated directly on the ice sheet from RACMO2 (Extended Data Fig. 5), suggesting that coastal temperature observations (some of which are far removed from the ice sheet) may poorly or only partially represent climatic and surface energy balance conditions over the ice sheet. Owing to observational paucity on the ice sheet proper, especially before the last two decades<sup>19</sup>, ice-core-derived melt records that directly capture melt processes are therefore of particularly high value.

**Quantifying significance of paired time series.** Statistical significance of correlations among air temperatures, melt records, and runoff reconstructions was assessed with a two-tailed Student's *t*-test (Fig. 2 inset; Extended Data Tables 2, 3). For analyses between paired time series smoothed with 5-year moving averages, we accounted for autocorrelation in the smoothed data using two distinct methods. First, following ref.<sup>52</sup>, we calculated reduced effective sample sizes,  $n^*$ , and thus reduced effective degrees of freedom (d.o.f.  $= n^* - 2$ ), given inherent lag-1 autocorrelation. As a secondary test of statistical significance given the presence of sample autocorrelation in the paired 5-year smoothed series, and following our reconstruction methods above, we also implemented a nonparametric Monte Carlo-based method<sup>42</sup> to generate 10,000 pseudo-random series with the exact length and autocorrelative properties of each time series. We then quantified correlations using these surrogate datasets against the original second time series, and estimated significance by calculating the exceedance probability of generating a stronger correlation by chance alone.

**Trend onset and emergence timing.** We examined the timing of the onset of the most recent phase of increasing GrIS meltwater runoff, as well as the emergence of GrIS runoff beyond a pre-industrial baseline, and compared these timings to those of reconstructed Arctic temperatures (that is, 'Arctic2k' in ref.<sup>21</sup>) and summer (July–September) sea ice extent<sup>29</sup> (Fig. 4b; Extended Data Table 4). For these analyses, we used the SiZer (Significant ZERO crossings of derivatives) method<sup>53</sup> following recent studies<sup>21,45</sup>, to calculate the median onset of sustained, significant ( $P < 0.1$ ) trends from smoothed time series of the original datasets using a suite of Gaussian kernel filters from 15 years to 50 years. Uncertainty in trend change-point timing is expressed here as the median absolute deviation of the change points determined using each of the 36 synthetic data series (smoothed using the 15–50-year filters). Next, we tested whether GrIS runoff has surpassed natural variability, commonly defined as  $+2\sigma$  beyond a pre-industrial period<sup>21,54</sup>. As in our assessments of the magnitude of melt increases, we defined the pre-industrial period for the Arctic temperature and runoff reconstruction datasets as the eighteenth century (1700–1799), which has been identified as a period predating the onset of industrial-era Arctic warming<sup>21</sup>. Emergence is defined here as the median timing at which the 15–50-year smoothed time series surpass and remain above the pre-industrial  $+2\sigma$  level. As with trend onset timing, we estimated uncertainty in emergence timing as the median absolute deviation in the emergence timings determined using the various filter widths. Timing and uncertainty range in trend onset and emergence timing for these and other data series are shown as the vertical lines and shaded regions in Fig. 4b, and expressed numerically in Extended Data Table 4.

We also evaluated the trend onset and emergence timing from an observationally derived sea-ice reconstruction by Walsh et al.<sup>29</sup> and compare this dataset

with a longer, proxy-derived summer sea ice reconstruction from Kinnard et al.<sup>30</sup>. To facilitate comparison, we performed a minor adjustment (that is, bias correction) by matching the mean of the Kinnard time series to the mean of the Walsh dataset over 1850–1899, a period of common overlap and of little sea-ice change, by subtracting  $0.22 \times 10^6 \text{ km}^2$  from the full Kinnard dataset. Likewise, we note that the lower temporal resolution (40-yr low-pass filtered) of the Kinnard dataset precluded accurate assessment of change points and emergence from this longer dataset. Owing to the shorter length (1850–present) of the observationally derived Walsh sea-ice reconstruction, it was necessary to define the baseline period for this dataset as 1850–1899. Nevertheless, we have confidence in our estimated timing of summer sea-ice decline and its forced emergence given the clear similarity of the observationally based and proxy-based sea-ice datasets (Fig. 4b). Because the Kinnard data show relatively stable summer sea ice before 1850, but with a slight decrease during the baseline period used for the other datasets (1700–1799), we believe our calculated climate emergence from the Walsh dataset to be a conservative estimate (that is, early in time). Indeed, if we utilize the bias-adjusted summer sea-ice extent from Kinnard over the earlier baseline of 1700–1799 with the standard deviation of the annual-resolution Walsh data (over 1850–1899), the median emergence is moved forward in time to  $1966 \pm 3$  years, still predating the median emergence of GrIS runoff by 10 yr.

**Nonlinear melt–temperature relationship.** We extracted profiles of melt and temperature at our coring sites and from an accumulation zone ( $>1,200 \text{ m}$ ) elevational transect spaced every 100 m down the centreline of basin 7.1, containing our three cores forming the CWG stack (outline shown in Fig. 1a; also Extended Data Fig. 6). Because RACMO2.3p2 and MARv3.7 represent different time spans and incorporate unique snow models, we used both in our assessment of melt–temperature sensitivity (Fig. 4c). For RACMO2.3p2, simulated melt at the NU core site was determined to be implausibly low (26.5 millimetres of water equivalent per year over 1994–2013) despite a relatively high air temperature over this time period ( $-1.52^\circ\text{C}$ ), and so we did not utilize this model at this site. In comparison, MARv3.7 simulates much greater melt (898 millimetres of water equivalent per year) and higher air temperature ( $-0.92^\circ\text{C}$ ) averaged over 1994–2013. These values align with the expected melt–temperature relationship derived from basin 7.1, but also greatly exceed accumulation rate determined from the NU core (around 300 millimetres of water equivalent per year). Because our analysis of the ice core chemistry and resulting dating do not indicate missing years (that is, net annual ablation), we believe MARv3.7 simulates unrealistically high melt at this site. We speculate that these discrepancies are at least partially due to the small size of the NU ice cap (about  $4 \text{ km} \times 4 \text{ km}$ ), its more maritime climate, and the relatively coarse grid scale of the native climate model simulations (11 km and 7.5 km for RACMO2 and MAR, respectively). Because our in situ observations reveal that the NU site experiences higher melt than our GrIS cores (and thus it more closely represents conditions along the margins of the GrIS where runoff is prevalent), we include surrogate melt and temperature points from RACMO2.3p2 and MARv3.7 for the NU core site. As a potential analogue for conditions at the NU core site, we plot in Fig. 4c values derived from 1,900 m along the centerline of basin 7.1, where simulated melt rates are consistent with those derived from our NU core. From these data, we find that an exponential function well represents the nonlinear relationship between surface melting and near-surface air temperature. This result is consistent with previous ice-core melt reconstructions<sup>26</sup> and model-based studies in Greenland<sup>55</sup> and Antarctica<sup>27</sup>.

To assess melt conditions associated with runoff initiation, using both RACMO2.3p2 and MARv3.7 we isolated melt flux values for the three highest-elevation sampling sites along the basin 7.1 centreline with multiple years of runoff simulated at  $>10$  millimetres of water equivalent per year. From these runoff-associated melt fluxes, we calculated the mean melt associated with initial runoff and the standard deviation among the mean melt fluxes (shown as dashed runoff line and shaded area in Fig. 4c). This level of melt linked to initial onset of runoff in recent years is a function of more frequent or sustained high-intensity melt that leads to formation of thicker refrozen melt layers before favouring runoff over retention<sup>8,56,57</sup>.

**Analysis of periodicities in ice-core melt records.** Semi-periodic oscillations are apparent in our primary ice-core-derived melt records (Fig. 2). To explore this variability more quantitatively, and to discern potential signatures of climate modes known to affect Greenland, we performed analyses to identify spectral signatures and coherence between our melt records and climate indicators including the North Atlantic Oscillation<sup>58</sup>, the Atlantic Multidecadal Oscillation, the Greenland Blocking Index<sup>59</sup>, and air temperatures. Extended Data Fig. 2 displays a subset of these analyses. The upper four plots show power spectral density using the multi-taper method<sup>60</sup> for our two main melt records and the summertime North Atlantic Oscillation and the Greenland Blocking Index, two atmospheric modes known to influence Greenland climate and melt<sup>14,23,59</sup>. We find relatively high spectral power in the 13–16-year range common to NU and CWG. This periodicity appears consistent with the North Atlantic Oscillation, which shows

moderate evidence of spectral energy centred around a periodicity of about 13 years, although the summertime North Atlantic Oscillation is characteristically noisy (Extended Data Fig. 2d). We also note a periodicity of about 8 years in CWG corresponding to moderately high power in the Greenland Blocking Index, and also previously described for the winter North Atlantic Oscillation<sup>59</sup> but not apparent here in the summertime North Atlantic Oscillation. Finally, we find strong, high spectral power at 60-year periodicity in our coastal ice cap record, NU, consistent with the known 60–80-year periodicity of Atlantic Multidecadal Oscillation<sup>61,62</sup>. Cross-wavelet analysis<sup>63</sup> reveals the greatest coherence and stationarity between the NU melt record and the southwest Greenland JJA air-temperature composite<sup>51</sup> (Extended Data Fig. 2e). This analysis reveals high common power in the ~10–25-yr range and generally in phase relationships, with periods of melt partially leading temperature that probably reflect meltwater percolation in this high-melt core.

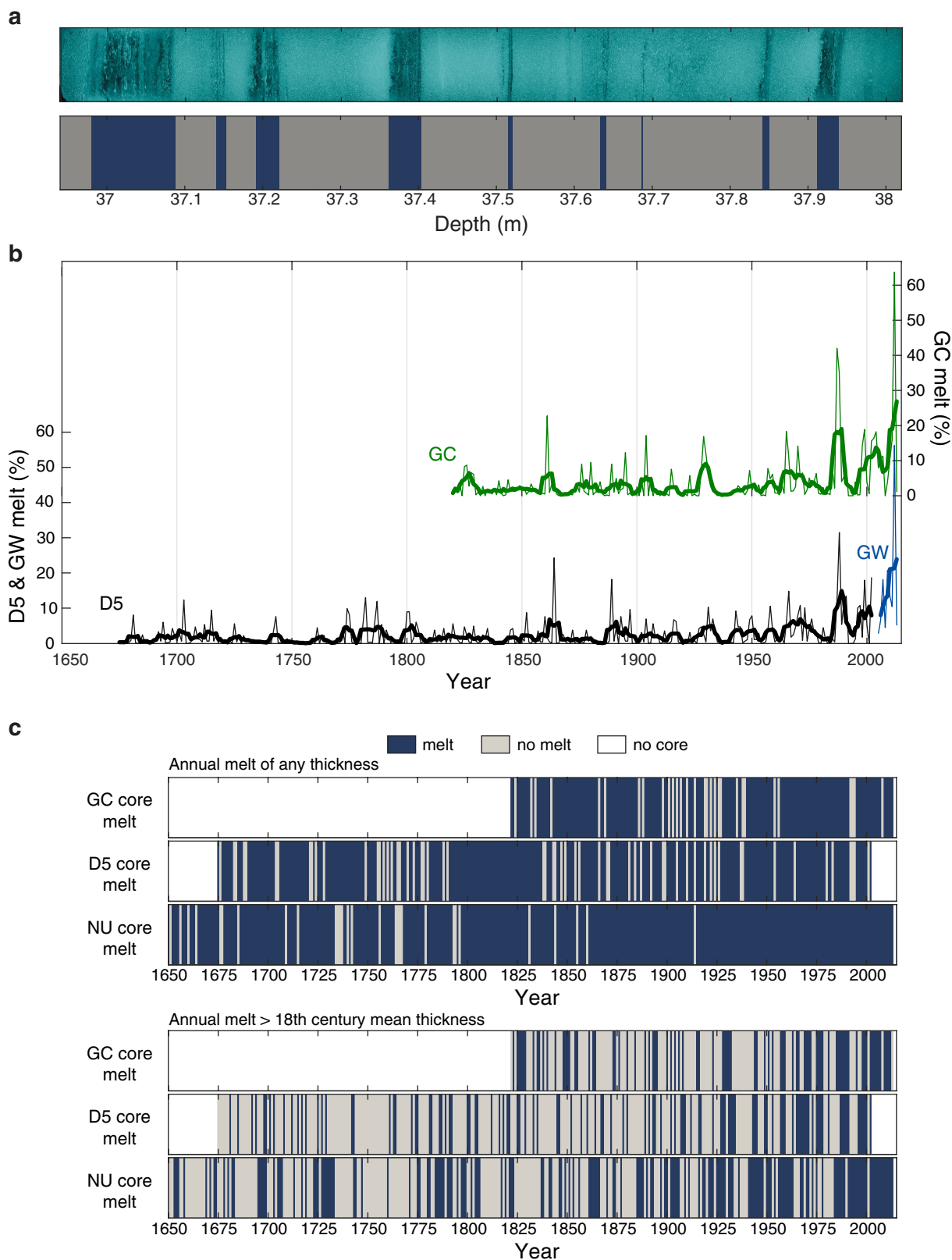
Our finding of strongest temporal coherence between NU and air temperature (as opposed to an individual climate mode) potentially indicates the combined influence of multiple climate modes on Greenland melt that are well represented by air temperature. Indeed, it is a confluence of processes that impact Greenland climate, combined with ice-sheet–climate interactions including the melt–albedo feedback, that govern the melt variability archived in ice cores. Given noise inherent to the relatively short time series, further analysis is warranted to better discern the varied factors responsible for the longer-term evolution of Greenland melt, and the representation of these processes in ice-core melt records.

**Code availability.** Code used for runoff reconstructions is available from L.D.T. upon request. Codes used for SiZer analysis were modified from ref. 23 (<https://www.nature.com/articles/nature19082>) and available from L.D.T. upon request.

### Data availability

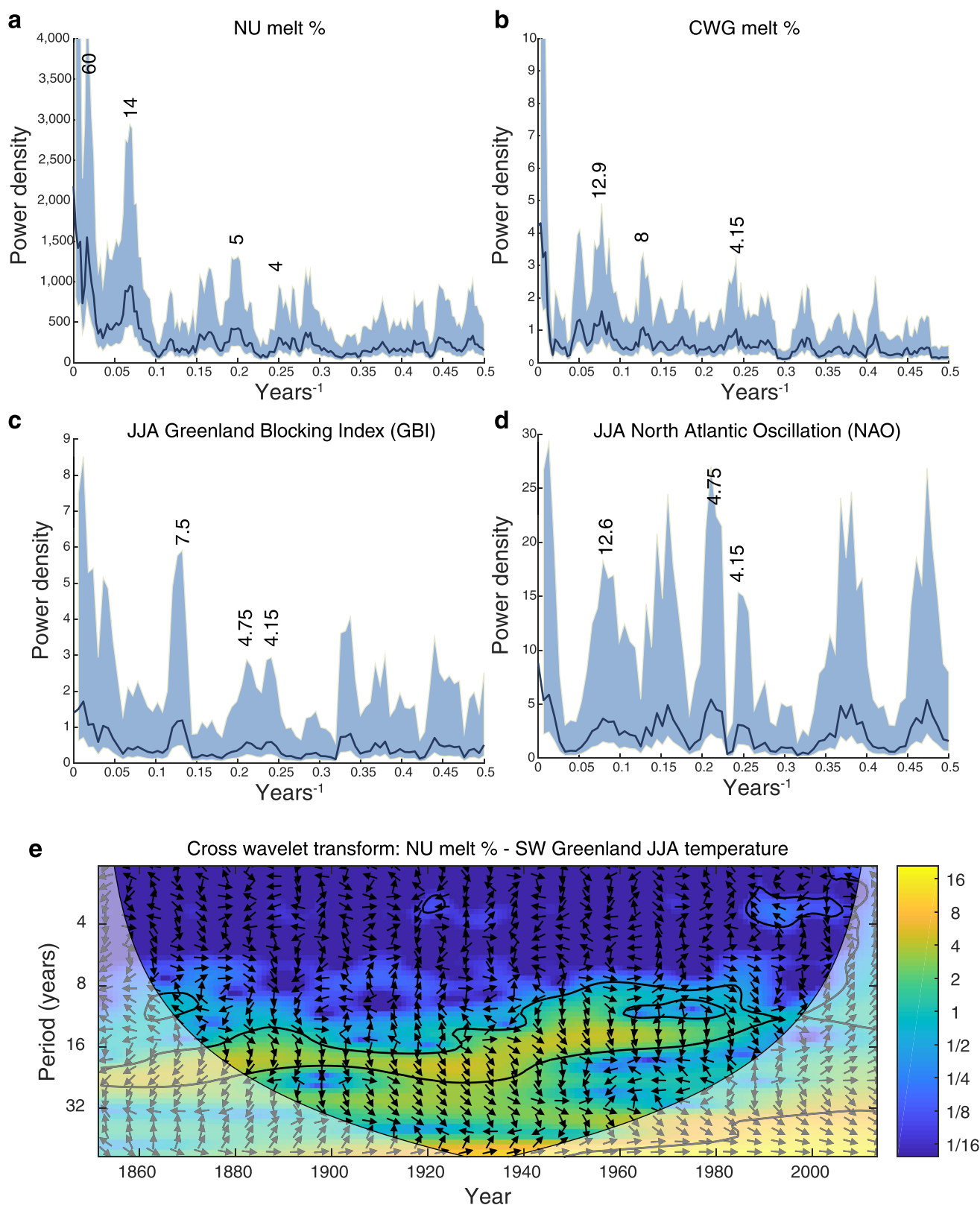
Ice-core melt records, the derived runoff reconstructions, and other records from cores NU, GC and GW are available via the NSF Arctic Data Center (<http://arcticdata.io>) and from the corresponding author upon request. Additionally, source data for Figs. 2, 4 are provided in the online version of this paper. RACMO2 model outputs<sup>5</sup> as well as downscaled 1-km surface mass balance data are available from B.P.Y.N. and M.R.v.d.B. upon request. MAR model outputs<sup>6</sup> are available from X.F. upon request. Greenland air-temperature data<sup>51</sup> are available from <http://www.dmi.dk/laer-om/generelt/dmi-publikationer/tekniske-rapporter/>. Sea-ice data<sup>29,30</sup> are available from <https://nsidc.org/data/g10010> and <https://www.nature.com/articles/nature10581>. Arctic air-temperature reconstruction data<sup>21</sup> are available from <https://www.nature.com/articles/nature19082>. Satellite melt data<sup>4,41</sup> are available from <http://www.cryocity.org>.

31. Curran, M. A. & Palmer, A. S. Suppressed ion chromatography methods for the routine determination of ultra low level anions and cations in ice cores. *J. Chromatogr. A* **919**, 107–113 (2001).
32. Sigl, M. et al. Timing and climate forcing of volcanic eruptions for the past 2,500 years. *Nature* **523**, 543–549 (2015).
33. McConnell, J. R., Lamorey, G. W., Lambert, S. W. & Taylor, K. C. Continuous ice-core chemical analyses using inductively coupled plasma mass spectrometry. *Environ. Sci. Technol.* **36**, 7–11 (2002).
34. McConnell, J. R. et al. 20th-century industrial black carbon emissions altered Arctic climate forcing. *Science* **317**, 1381–1384 (2007).
35. Gfeller, G. et al. Representativeness and seasonality of major ion records derived from NEEEM firn cores. *Cryosphere* **8**, 1855–1870 (2014).
36. Arienzo, M. M. et al. A method for continuous <sup>239</sup>Pu determinations in Arctic and Antarctic ice cores. *Environ. Sci. Technol.* **50**, 7066–7073 (2016).
37. McGwire, K. C. et al. An integrated system for optical imaging of ice cores. *Cold Reg. Sci. Technol.* **53**, 216–228 (2008).
38. Das, S. B. & Alley, R. B. Characterization and formation of melt layers in polar snow: observations and experiments from West Antarctica. *J. Glaciol.* **51**, 307–312 (2005).
39. Das, S. B. & Alley, R. B. Rise in frequency of surface melting at Siple Dome through the Holocene: evidence for increasing marine influence on the climate of West Antarctica. *J. Geophys. Res.* **113**, D02112 (2008).
40. Noël, B. et al. A daily, 1 km resolution data set of downscaled Greenland ice sheet surface mass balance (1958–2015). *Cryosphere* **10**, 2361–2377 (2016).
41. Tedesco, M. *Greenland Daily Surface Melt 25km EASE-Grid [1988-2013]* <http://www.cryocity.org/data.html> (City University of New York, New York, 2014).
42. Ebisuzaki, W. A method to estimate the statistical significance of a correlation when the data are serially correlated. *J. Clim.* **10**, 2147–2153 (1997).
43. Macias-Fauria, M., Grinsted, A., Helama, S. & Holopainen, J. Persistence matters: estimation of the statistical significance of paleoclimatic reconstruction statistics from autocorrelated time series. *Dendrochronologia* **30**, 179–187 (2012).
44. Cook, E. R., Briffa, K. R. & Jones, P. D. Spatial regression methods in dendroclimatology: a review and comparison of two techniques. *Int. J. Climatol.* **14**, 379–402 (1994).
45. Tierney, J. E. et al. Tropical sea surface temperatures for the past four centuries reconstructed from coral archives. *Paleoceanography* **30**, 2014PA002717 (2015).
46. Anchukaitis, K. J. et al. Last millennium Northern Hemisphere summer temperatures from tree rings. Part II, spatially resolved reconstructions. *Quat. Sci. Rev.* **163**, 1–22 (2017).
47. Zwally, H. J., Giovinetto, M. B., Beckley, M. A. & Saba, J. L. *Antarctic and Greenland Drainage Systems* [http://icesat4.gsfc.nasa.gov/cryo\\_data/ant\\_grm\\_drainage\\_systems.php](http://icesat4.gsfc.nasa.gov/cryo_data/ant_grm_drainage_systems.php) (GSFC Cryospheric Sciences Laboratory, NASA 2012).
48. Fisher, D. et al. Recent melt rates of Canadian arctic ice caps are the highest in four millennia. *Glob. Planet. Change* **84**, 3–7 (2012).
49. Vernon, C. L. et al. Surface mass balance model intercomparison for the Greenland ice sheet. *Cryosphere* **7**, 599–614 (2013).
50. Vinther, B. M., Andersen, K. K., Jones, P. D., Briffa, K. R. & Cappelen, J. Extending Greenland temperature records into the late eighteenth century. *J. Geophys. Res.* **111**, D11105 (2006).
51. Cappelen, J. (ed) *Greenland—DMI Historical Climate Data Collection 1784-2017 DMI Report 18-04* (DMI, Copenhagen, 2018).
52. Bretherton, C. S., Widmann, M., Dymnikov, V. P., Wallace, J. M. & Bladé, I. The effective number of spatial degrees of freedom of a time-varying field. *J. Clim.* **12**, 1990–2009 (1999).
53. Hannig, J. & Marron, J. S. Advanced distribution theory for SiZer. *J. Am. Stat. Assoc.* **101**, 484–499 (2006).
54. Hawkins, E. & Sutton, R. Time of emergence of climate signals. *Geophys. Res. Lett.* **39**, L01702 (2012).
55. Fettweis, X. et al. Estimating the Greenland ice sheet surface mass balance contribution to future sea level rise using the regional atmospheric climate model MAR. *Cryosphere* **7**, 469–489 (2013).
56. de la Peña, S. et al. Changes in the firn structure of the western Greenland Ice Sheet caused by recent warming. *Cryosphere* **9**, 1203–1211 (2015).
57. Noël, B. et al. A tipping point in refreezing accelerates mass loss of Greenland's glaciers and ice caps. *Nature Commun.* **8**, 14730 (2017).
58. Hurrell, J. & National Center for Atmospheric Research Staff (eds) *The Climate Data Guide: Hurrell North Atlantic Oscillation (NAO) Index (station-based)*. <https://climatedataguide.ucar.edu/climate-data/hurrell-north-atlantic-oscillation-nao-index-station-based> (NCAR, Boulder, 2003).
59. Hanna, E., Cropper, T. E., Hall, R. J. & Cappelen, J. Greenland Blocking Index 1851–2015: a regional climate change signal. *Int. J. Climatol.* **36**, 4847–4861 (2016).
60. Mann, M. E. & Lees, J. M. Robust estimation of background noise and signal detection in climatic time series. *Clim. Change* **33**, 409–445 (1996).
61. Schlesinger, M. E. & Ramankutty, N. An oscillation in the global climate system of period 65–70 years. *Nature* **367**, 723–726 (1994).
62. Trenberth, K. E. & Shea, D. J. Atlantic hurricanes and natural variability in 2005. *Geophys. Res. Lett.* **33**, L12704 (2006).
63. Grinsted, A., Moore, J. C. & Jevrejeva, S. Application of the cross wavelet transform and wavelet coherence to geophysical time series. *Nonlinear Process. Geophys.* **11**, 561–566 (2004).



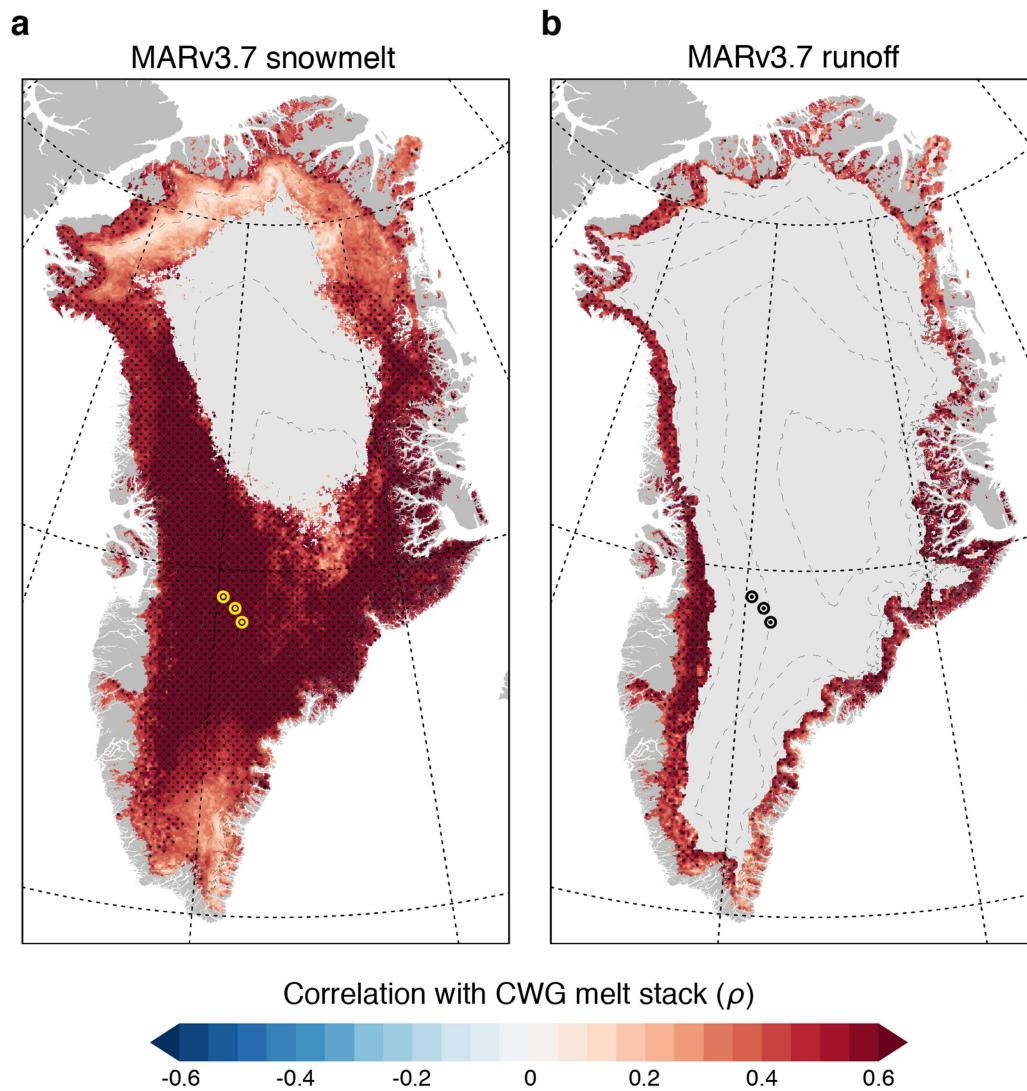
**Extended Data Fig. 1 | Example core section and additional annual melt records.** **a**, Example core scan image (top) and resulting digitized melt layers in blue (bottom). **b**, Annual melt per cent time series for cores in the CWG stack. Bold lines show 5-year moving averages. See Fig. 1 for locations. **c**, The top panel shows the presence (blue) or absence (grey) of any amount of refrozen surface melt within a particular year in our three longest ice cores, showing regular annual occurrence of melt at each

location. The bottom panel shows that, when filtered to show only years with melt percentages greater than the eighteenth-century mean melt at each site, a pattern towards recently more frequent, thicker (and thus more intense) melt emerges. As core GC does not span the eighteenth century, the mean eighteenth-century melt from the nearby D5 core was used as a baseline for GC as well.



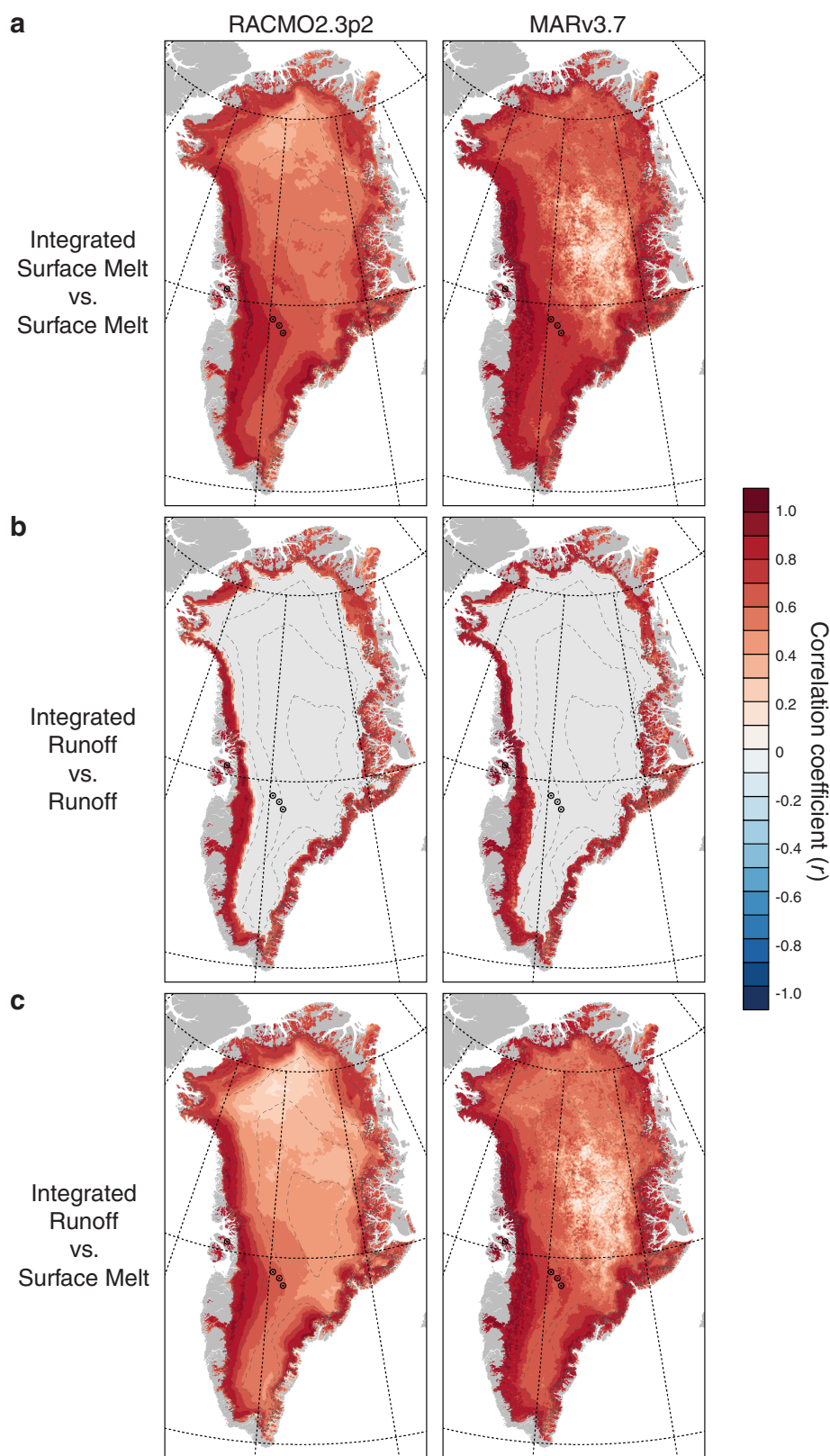
**Extended Data Fig. 2 | Analysis of spectral signatures in melt and climate records.** **a–d**, Multi-taper method spectral power plots for our ice cores, the Greenland Blocking Index<sup>59</sup> and the North Atlantic Oscillation<sup>58</sup>. **e**, Cross-wavelet transform plot between NU melt and southwest Greenland temperatures<sup>51</sup>. In the spectral plots (**a–d**), years corresponding to specific peaks in spectral power are indicated by numbers, although many peaks are surrounded by a range of years with elevated spectral power. Shaded areas represent 95% confidence bounds, and we note that many peaks do not show up significantly (5% confidence) above a white-noise threshold. In the cross-wavelet plot in **e**, areas of

significant ( $P < 0.05$ ) coherence are surrounded by a black line. The white-shaded areas represent regions where coherence cannot be confidently established owing to edge effects. Arrows indicate phase relationships: rightward (leftward) arrows indicate in-phase (out-of-phase) relationships, while downward (upward) arrows indicate melt leading (lagging) temperature. Our analyses found the strongest, and generally in-phase, coherence between NU and air temperature, as opposed to a single climate index, suggestive of the combined influence of multiple climate modes on GrIS melt that are well represented by air temperature (Methods).



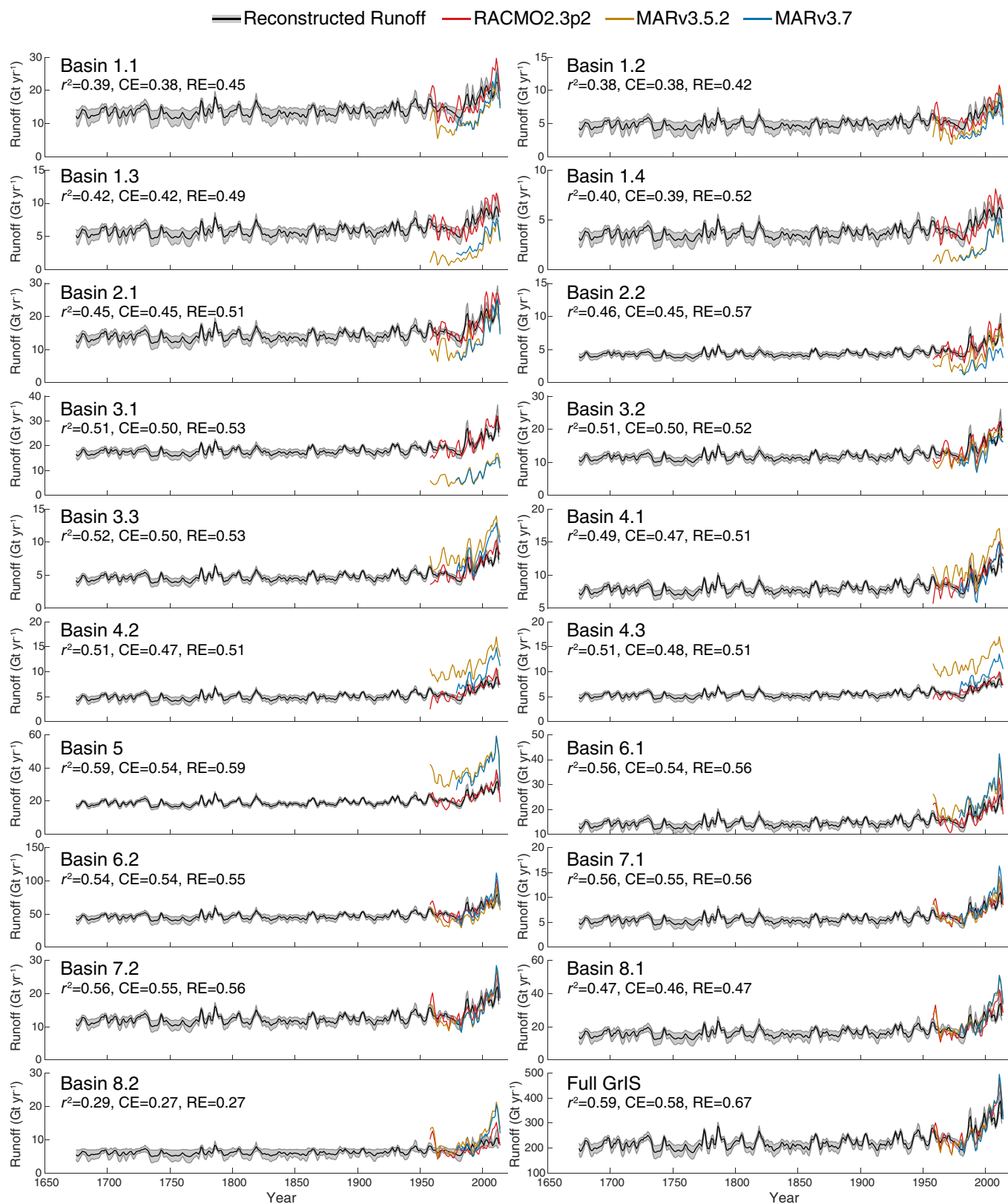
**Extended Data Fig. 3 | Further evidence of spatially broad representation of melt processes in CWG cores.** Spearman rank order correlations between the CWG melt stack and MARv3.7-modelled annual snowmelt (**a**) and snowmelt runoff (**b**) over the period 1978–2013. As in correlations against RACMO2 and satellite melt (Fig. 3), correlations

here are shown only for areas where MAR-simulated melt or runoff in at least 50% of the years of common overlap between the core and modelled datasets (18 years). Areas of significant correlation ( $P < 0.01$ ) are denoted by a stipple pattern. Locations of cores used in the CWG stack are denoted by yellow (**a**) or black (**b**) points.



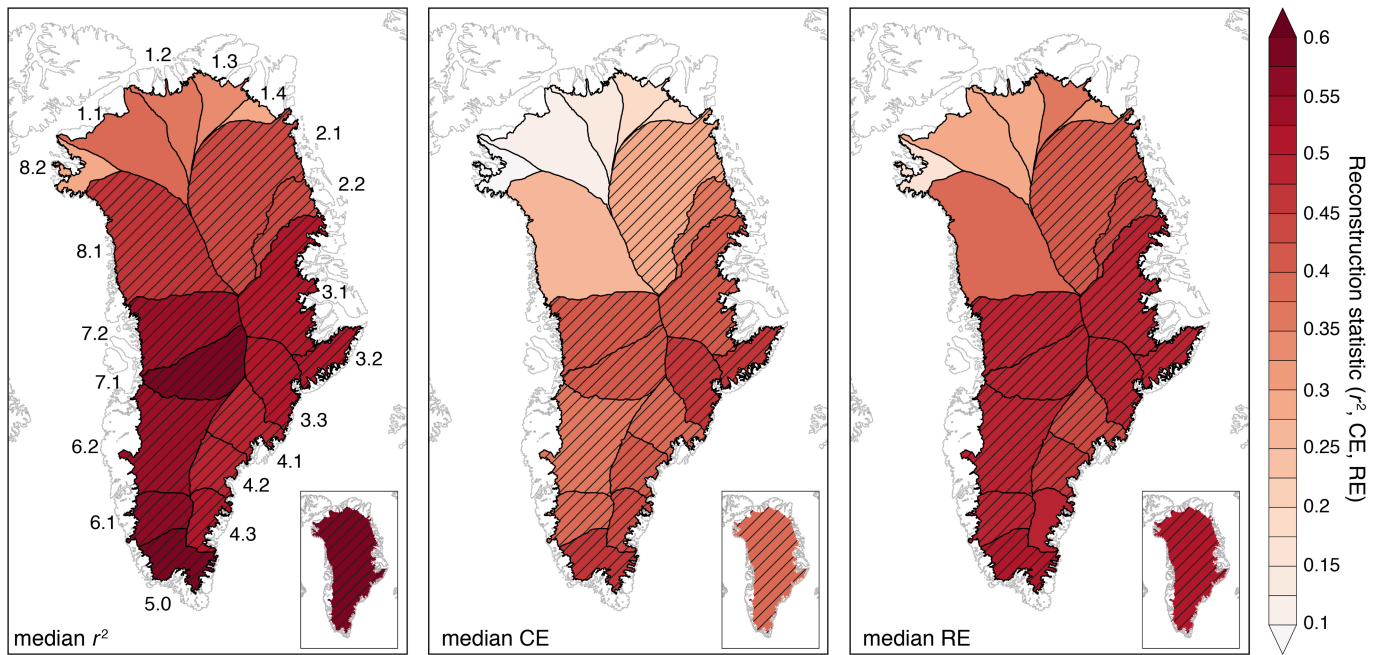
**Extended Data Fig. 4 | Relationships between local and ice-sheet-integrated melt processes.** Pearson correlation coefficients ( $r$ ) between GrIS-integrated surface melt and surface melt in each grid cell (a), GrIS-integrated runoff and runoff in each grid cell (b), and GrIS-integrated runoff and surface melt in each grid cell (c). Correlations calculated for RACMO2.3p2 over 1958–2013 (left-hand plots) and

MARv3.7 over 1979–2013 (right-hand plots). Interannual variability in GrIS-integrated melt/runoff is well represented by local-scale interannual variability in melt/runoff. In situ melt records (for example, from well sited percolation-zone ice cores that are able to capture interannual melt variability) can therefore be used to quantify GrIS-integrated melt and runoff.



**Extended Data Fig. 5 | Basin-specific runoff reconstructions.** Reconstructed runoff using the NU and CWG ice-core melt records calibrated to RACMO2.3p2 for 19 surface drainage basins<sup>47</sup> and for the full GrIS by summing each basin (lower right; as in Fig. 4). Note unique vertical axes. Reconstruction statistics shown are the maximum

values achieved for each metric across 20 stepwise calibration/validation intervals. Shaded regions around runoff reconstruction represent 95% confidence bounds. Modelled datasets smoothed using a 5-year Lowess filter. For details on reconstruction see Methods and see Extended Data Fig. 6 for basin location and further statistical assessment.



**Extended Data Fig. 6 | Basin-specific and GrIS-integrated reconstruction statistics.** Median values of runoff reconstruction skill statistics ( $r^2$ , CE, RE) over 20 stepwise calibration/validation intervals, calculated for each surface drainage basin (basin numbers in left-hand plot), and for the GrIS as a whole (inset plots). Hatching denotes areas

where at least half of the calibration/validation intervals were found to be statistically significant at the  $P < 0.1$  level, determined using 10,000 Monte Carlo simulations (see Methods). All basins had at least one calibration/validation interval where at least one of the three validation statistics was significant. See Methods for details on reconstruction methods.

**Extended Data Table 1 | Details of firn and ice cores used in this study**

| Core | Year collected | Longitude | Latitude | Elevation (m a.s.l.) | Length (m) | Reference                        |
|------|----------------|-----------|----------|----------------------|------------|----------------------------------|
| GC   | 2015           | -43.5025  | 68.892   | 2436                 | 104        | This study                       |
| GW   | 2014           | -44.5198  | 69.2028  | 2291                 | 9          | This study                       |
| NU   | 2015           | -52.2641  | 70.4865  | 1950                 | 140        | This study                       |
| D5   | 2003           | -42.9     | 68.5     | 2515                 | 148        | McConnell et al., 2007 (ref. 34) |

m.a.s.l., metres above sea level. The core source is from ref. <sup>34</sup>.

**Extended Data Table 2 | Statistical relationships among ice cores and CWG air temperature**

| Correlation series                                | Annual/seasonal data      | 5-yr moving averages        |
|---|---------------------------|-----------------------------|
| CWG melt versus JJA air temperature <sup>50</sup> | $r = 0.331$ ( $n = 170$ ) | $r = 0.581$ ( $n^* = 95$ )  |
| NU melt versus JJA air temperature <sup>50</sup>  | $r = 0.259$ ( $n = 170$ ) | $r = 0.639$ ( $n^* = 91$ )  |
| CWG melt versus NU melt                           | $r = 0.308$ ( $n = 339$ ) | $r = 0.660$ ( $n^* = 188$ ) |

All correlations are significant at  $P < 0.01$  level. For 5-year moving average time series, statistical significance was tested using reduced effective number of observations ( $n^*$ ), as well as with a Monte Carlo-based procedure, to account for sample autocorrelation (Methods). Temperature data are from ref. <sup>50</sup> as shown.

**Extended Data Table 3 | Statistical relationships among ice cores, reconstructed runoff and pan-Greenland air temperatures**

| Observational record                            | Combined CWG and NU melt time series | Reconstructed runoff from adjacent basin(s)      |
|---|--------------------------------------|--|
|   | Multiple $r$                         | $r$ / Runoff time series                         |
| Danmarkshavn (1949–2013)                        | 0.839 ( $n = 65$ )                   | <b>0.766</b> ( $n^* = 39$ ) / Basin 2.1          |
| Ilulissat <sup>†</sup> (1850–2013)              | 0.665 ( $n = 174$ )                  | <b>0.641</b> ( $n^* = 96$ ) / Basin 7.1          |
| Ittoqqortoormiit (1949–2013)                    | 0.767 ( $n = 65$ )                   | <b>0.701</b> ( $n^* = 36$ ) / Basin 3.2          |
| Ivituut / Narsarsuaq (1873–2013)                | 0.634 ( $n = 114$ )                  | <b>0.599</b> ( $n^* = 79$ ) / Basin 5            |
| Nuuk <sup>†</sup> (1866–2013)                   | 0.543 ( $n = 148$ )                  | <b>0.520</b> ( $n^* = 82$ ) / Basin 6.1          |
| Pituffik (1948–2013)                            | 0.545 ( $n = 66$ )                   | 0.482 ( $n^* = 37$ ) / Basin 8.2                 |
| Tasiilaq (1895–2013)                            | 0.348 ( $n = 119$ )                  | 0.261 <sup>§</sup> ( $n^* = 64$ ) / Basin 4.2    |
| Upemavik (1871–2013)                            | 0.690 ( $n = 141$ )                  | <b>0.643</b> ( $n^* = 77$ ) / Basin 8.1          |
| Qaqortoq <sup>†</sup> (1873–2013)               | 0.463 ( $n = 141$ )                  | <b>0.418</b> ( $n^* = 79$ ) / Basin 5            |
| SW Greenland composite <sup>‡</sup> (1840–2013) | 0.595 ( $n = 174$ )                  | <b>0.566</b> ( $n^* = 95$ ) / Basins 5, 6.1, 7.1 |

All series smoothed using a 5-year moving average to account for noise inherent to ice-core melt records. The second column shows correlations (multiple  $r$  values) using CWG and NU melt records as predictor variables against the indicated temperature time series, with all regressions significant at  $P < 0.01$ . The third column shows local correlations between our runoff reconstruction in the indicated basin(s) and the nearby temperature observations. For these series, we assessed significance using the reduced effective number of observations,  $n^*$ , accounting for serial correlation. All regressions are significant at  $P < 0.01$  using  $n^* - 2$  degrees of freedom, except for Tasiilaq<sup>‡</sup>. Relationships in bold were further found to be statistically significant assuming  $P < 0.05$  using a Monte Carlo-based approach (see Methods for details).

<sup>†</sup>Includes infilled and regressed observations from regional stations<sup>50,51</sup>.

<sup>‡</sup>Synthesis of Ilulissat, Nuuk and Qaqortoq master records<sup>50,51</sup>.

<sup>§</sup> $P = 0.037$  (using  $n^* - 2$  degrees of freedom; see Methods).

**Extended Data Table 4 | Timing of trend initiation and climate emergence**

| Climate record                        | Trend onset            | Climate emergence    |
|---------------------------------------|------------------------|----------------------|
| Arctic2k air temperatures (ref. 23)   | 1830.5 (1828–1833)     | 1937.5 (1936–1939)   |
| Greenland runoff (full GrIS)          | 1865 (1857.5–1872.5)   | 1976 (1974–1978)     |
| Arctic summer (JAS) sea ice (ref. 29) | 1878.5 (1857.5–1899.5) | 1947 (1943–1951)     |
| Basin 1.1 reconstructed runoff        | 1865 (1858.5–1871.5)   | 1980.5 (1979–1982)   |
| Basin 1.2 reconstructed runoff        | 1865 (1858.5–1871.5)   | 1983.5 (1983–1984)   |
| Basin 1.3 reconstructed runoff        | 1865 (1858.5–1871.5)   | 1984 (1984–1984)     |
| Basin 1.4 reconstructed runoff        | 1865 (1858.5–1871.5)   | 1984 (1983–1985)     |
| Basin 2.1 reconstructed runoff        | 1865 (1857.5–1872.5)   | 1976 (1974–1978)     |
| Basin 2.2 reconstructed runoff        | 1870 (1857–1883)       | 1969.5 (1966–1973)   |
| Basin 3.1 reconstructed runoff        | 1868 (1858–1878)       | 1970.5 (1967–1974)   |
| Basin 3.2 reconstructed runoff        | 1867 (1857.5–1867.5)   | 1971.5 (1968–1975)   |
| Basin 3.3 reconstructed runoff        | 1866 (1858–1874)       | 1974 (1971.5–1976.5) |
| Basin 4.1 reconstructed runoff        | 1866 (1858–1874)       | 1975 (1972–1978)     |
| Basin 4.2 reconstructed runoff        | 1865 (1858.5–1871.5)   | 1979 (1977–1981)     |
| Basin 4.3 reconstructed runoff        | 1865 (1858.5–1871.5)   | 1981 (1980–1982)     |
| Basin 5.0 reconstructed runoff        | 1865 (1858.5–1871.5)   | 1977.5 (1975–1980)   |
| Basin 6.1 reconstructed runoff        | 1865 (1857.5–1872.5)   | 1976 (1974–1978)     |
| Basin 6.2 reconstructed runoff        | 1865 (1857.5–1872.5)   | 1975.5 (1973–1978)   |
| Basin 7.1 reconstructed runoff        | 1865 (1857.5–1872.5)   | 1976 (1973.5–1978.5) |
| Basin 7.2 reconstructed runoff        | 1865 (1857.5–1872.5)   | 1976 (1974–1978)     |
| Basin 8.1 reconstructed runoff        | 1865 (1857.5–1872.5)   | 1977 (1975–1979)     |
| Basin 8.2 reconstructed runoff        | 1865 (1858.5–1871.5)   | 1981 (1979–1983)     |

Onset of significant trends and climate emergence above pre-industrial levels is defined as 1700–1799 (median and range expressed as  $\pm$ median absolute deviation) for datasets shown in Fig. 4b (first three records) and for basin-level runoff reconstructions shown in Extended Data Fig. 5. Temperature and sea-ice data are from refs <sup>23,29</sup>.